JGR Oceans

RESEARCH ARTICLE
10.1029/2022JC019535

Influence of Shelf Break Processes on the Transport of Warm Waters Onto the Eastern Amundsen Sea Continental Shelf

Marina Azaneu[1], Benjamin Webber[1], Karen J. Heywood[1], Karen M. Assmann[2,3], Tiago S. Dotto[1,4], and E. Povl Abrahamsen[5]

[1]Centre for Ocean and Atmospheric Sciences, School of Environmental Sciences, University of East Anglia, Norfolk, UK, [2]Institute of Marine Research, Tromsø, Norway, [3]Department of Marine Sciences, University of Gothenburg, Gothenburg, Sweden, [4]National Oceanography Centre, Southampton, United Kingdom, [5]British Antarctic Survey, Natural Environment Research Council, Cambridge, UK

Key Points:

- Zonal wind stress changes north of the shelf break drive different Circumpolar Deep Water (CDW) varieties onto the eastern Amundsen Sea continental shelf
- Heat content, on-shore flow, and heat flux co-vary strongly between central and eastern continental troughs
- The 2015/2016 El Niño led to stronger onshore heat flux, despite the lower onshore temperatures due to upwelling of colder CDW variety

Correspondence to:
M. Azaneu,
m.azaneu@uea.ac.uk

Citation:
Azaneu, M., Webber, B., Heywood, K. J., Assmann, K. M., Dotto, T. S., & Abrahamsen, E. P. (2023). Influence of shelf break processes on the transport of warm waters onto the eastern Amundsen Sea continental shelf. *Journal of Geophysical Research: Oceans*, *128*, e2022JC019535. https://doi.org/10.1029/2022JC019535

Received 1 DEC 2022
Accepted 2 MAY 2023

Abstract The heat transported onto the continental shelf by Circumpolar Deep Water (CDW) is the main driver of ice shelf basal melting in the Amundsen Sea. Here, we investigate the slope current system and the variability of the heat transported through the Pine Island-Thwaites central and eastern troughs using data from five moorings deployed in the region between 5 March 2012 and 7 February 2016. Substantial variability on intermonthly time scales (3–4 months) is observed in the onshore heat flux, driven primarily by zonal wind stress north of the shelf break. Heat content, onshore flow, and heat flux are highly correlated between central and eastern troughs, which are most likely dynamically linked by the zonal wind stress forcing. This is the first time this dynamic link between troughs is observed. In the eastern the Amundsen Sea, during the El Niño of 2015/2016, strong eastward winds led to lower temperatures over the continental shelf while the onshore heat flux is intensified. We hypothesize that this anti-correlation between heat content and heat flux results from a strengthened eastward undercurrent leading to upwelling of a colder and deeper CDW variety. These results highlight the complex and heterogeneous response of this region to environmental and the importance of velocity data for understanding the dynamics in this region. It also suggests that the hypothesized link between large-scale atmospheric forcing (e.g., El Niño-Southern Oscillation) and ice-shelf melt is not produced via changes in heat content, but instead via changes in onshore heat flux.

Plain Language Summary Heat stored in the ocean is the main reason that floating ice attached to the glaciers that surround the Amundsen Sea is melting. We investigate how the strength of coastal currents and the amount of heat transported by them toward the Antarctic shore vary in time. We use continuous measurements for up to 4 yr of ocean currents at five different locations in the Amundsen Sea. The amount of heat transported by a relatively warm current varies mostly with a 3–4 months period, which is influenced by local surface winds. These are the first observations showing consistency in the variability of heat transported toward the shore across different locations in this region. Moreover, we show that changes in the local winds related to the El Niño event of 2015/2016 led to a period of low ocean temperatures and enhanced transport of heat toward the shore. We explain this contradictory behavior as a result of a stronger flow of deeper, colder waters influenced by stronger westerly winds. This suggests that the rate at which heat is transported toward the shore is likely more important than the temperature of the water in determining the melting of glaciers around the Amundsen Sea.

1. Introduction

Ocean-induced basal melting is the main cause of thinning and grounding line retreat of glaciers draining the Amundsen Sea sector of the West Antarctic Ice Sheet during recent decades (Rignot et al., 2019; Smith et al., 2020). Pine Island and Thwaites Glaciers are two of the major ice streams flowing into the eastern Amundsen Sea Embayment. Despite the previous fast retreat, the ice discharge of Pine Island Glacier remained steady between 2009 and 2013, and its grounding line retreat stagnated (Mouginot et al., 2014), partially due to relatively cold ocean conditions (Konrad et al., 2018; Webber et al., 2017). This cold period led to lower basal melt rates in comparison with historical data (Heywood et al., 2016). Despite the stabilization in the mass loss rate, Pine Island is still one of the largest contributors (58 Gt/yr) to Antarctic mass loss (Rignot et al., 2019).

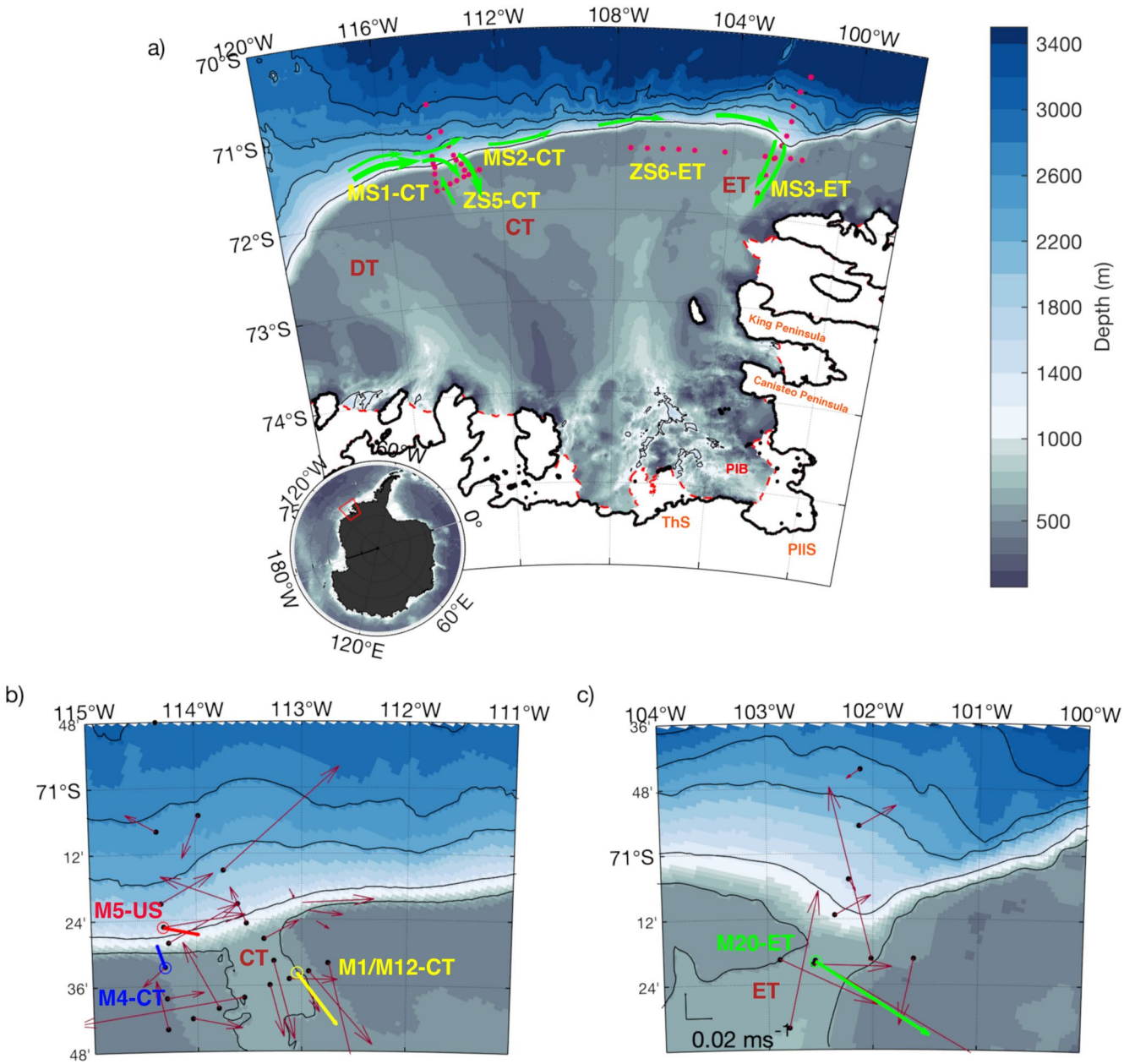

Figure 1. (a) Bathymetry of study area (shaded, with 1,200, 2,200, 2,600, and 3,000 m isobaths as thin black lines), ice shelf fronts (dashed red lines) and grounding zones (thick black lines) from BedMachine v2 (Morlighem et al., 2020), identifying Thwaites Glacier (ThS), Pine Island Ice Shelf (PIIS), Pine Island Bay (PIB), Dotson-Getz trough (DT), central (CT), and eastern (ET) troughs. CTD/LADCP stations (red dots) are collated into meridional (MS1-CT, MS2-CT, MS3-ET) and zonal (ZS5-CT, ZS6-ET) sections. Green schematic arrows depict general circulation at the upper slope and troughs. Inset map shows location of study area. Panels (b and c) show central and eastern troughs in more detail, with 600 m isobath also contoured. Dark red arrows indicate 300–700 m average LADCP velocities ($m\,s^{-1}$). (b) Yellow, blue, red and (c) green arrows indicate whole-record-means of depth-averaged current meter velocities from moorings M1/M12-CT, M4-CT, M5-US, and M20-ET, respectively.

Over the eastern Amundsen Sea continental shelf, the depth of the permanent thermocline and the associated average temperature below the depth of the base of the ice shelf (350 m) are often used as proxies for the amount of heat available within the sub-ice cavity for melting of the Pine Island Ice Shelf (PIS; Dutrieux et al., 2014; Jenkins et al., 2010). The overall increase in the on-shelf heat content is ultimately driven by the import of CDW onto the shelf (Holland et al., 2019; Jenkins et al., 2016), which is characterized by a subsurface temperature maximum above 1.5°C off-shelf. CDW accesses the continental shelf mainly through the central (113°W) and eastern (102°–108°W) troughs (Figure 1), where this water mass fills the ocean layer below 400 m (Nakayama

et al., 2013; Walker et al., 2007). The central and eastern troughs merge further on-shelf, allowing the inflow of both troughs to eventually mix and fill the deep Pine Island Bay (Jacobs et al., 2011; Nakayama et al., 2019). We term this the Central Trough to be consistent with previous studies (e.g., Assmann et al., 2013; Webber et al., 2019), but it should be noted that the same trough is named the Western Trough in some papers focusing on the eastern Amundsen Sea (e.g., Dutrieux et al., 2014). After intruding onto the continental shelf, CDW is modified by mixing with colder surface waters and is then referred to as modified CDW (mCDW). The importance of the contribution of each trough to the amount of heat that reach the ice shelves is, however, still debated (e.g., Assmann et al., 2013; Nakayama et al., 2013).

The along-slope current system in the eastern Amundsen Sea involves a westward geostrophic flow at the surface (Antarctic Slope Current), and a strong eastward undercurrent that has been previously described by Walker et al. (2013) and successfully represented by modeling studies (e.g., Assmann et al., 2013; Kimura et al., 2017). Such an undercurrent may arise in a situation of a downwelling system associated with the easterly winds driving the westward surface slope current, and set up initially by coastally trapped waves (Chavanne et al., 2010). The interaction of the eastward geostrophic undercurrent with the shelf break troughs is thought to facilitate the access of CDW to the continental shelf, providing a persistent south-eastward baroclinic flow of warm waters (St-Laurent et al., 2013). Among the mechanisms that have been suggested to explain the onshore transport of these warm waters through the troughs are topographic steering and the development of a dominant cyclonic flow from vortex stretching, the development and cyclonic propagation of topographic waves (St-Laurent et al., 2013), surface-forced upwelling induced by along-slope winds (Thoma et al., 2008) and upslope transport in the bottom Ekman layer (Wåhlin et al., 2012).

The pattern of winds at the continental shelf break is a result of multi-scale atmosphere-ocean interactions, both local and remote (Dutrieux et al., 2014; Holland et al., 2019; Steig et al., 2012). Surface winds can affect ocean conditions on different time scales by influencing the variability of the CDW inflow onto the shelf (Dutrieux et al., 2014; Kimura et al., 2017; Thoma et al., 2008; Webber et al., 2019), and surface buoyancy fluxes, which ultimately will determine the depth of the thermocline over the continental shelf (Jenkins et al., 2016; St-Laurent et al., 2015). For example, the connection between local winds and tropical atmospheric anomalies has been explored by Dutrieux et al. (2014) to explain a cool period over the Pine Island Bay under La Niña conditions, during which stronger westward zonal wind anomalies were associated with downwelling close to the continental shelf and limited access of CDW.

There are many factors that will mediate the effect of the winds on the oceanic conditions. For example, sea-ice coverage can impact the transfer of momentum from the atmosphere to the ocean surface and consequently may influence the variability of the on-shelf flow of CDW (Kim et al., 2017). The oceanic dynamic response to changes in winds in terms of strength and direction of the undercurrent can also impact the on-shelf heat transport on time scales shorter than those associated with large-scale atmospheric forcing (Assmann et al., 2013; St-Laurent et al., 2013). Furthermore, local atmospheric forcing strongly modulates the ocean within Pine Island Bay at depths critical for melting of the ice shelf (Davis et al., 2018; St-Laurent et al., 2015; Webber et al., 2017). As a consequence, the impact of the ocean circulation and local winds at the shelf break on ocean conditions close to the PIIS is not straightforward. Nevertheless, the variability of the CDW flow onto the continental shelf needs to be fully investigated as it is an important factor in determining the amount of heat available within the Amundsen Sea Embayment to drive ice shelf melting. There is still uncertainty on what causes this flow of warm water to vary, at what time scales and the impact on conditions further onshore.

In this study, we analyze a comprehensive data set that includes observations from five moorings (continuous measurements of up to ∼4 yr) and from ship-based hydrographic sections at the shelf break in the Amundsen Sea during February–March 2014. We present the first moored observations of the eastern trough hydrography, which allows the first assessment of the co-variability at the central and eastern troughs in the eastern Amundsen Sea. Using this unique data set, we investigate shelf break processes, including the slope current system, and its influence on the variability of the amount of heat transported onto the eastern Amundsen Sea continental shelf from weekly to interannual time scales.

The data set and calculations used here are presented in Section 2. Section 3 presents a snapshot of the mass and heat transports estimated from hydrographic sections sampled during an early 2014 research cruise as part of the iSTAR program (Investigating the Stability of the West Antarctic Ice Sheet). To set these values in context, Section 4 presents estimates of heat transport calculated from moored time series. The variability of the heat flux

at the shelf break and within the troughs is discussed in Section 5 based on mooring records of current velocity, temperature, and salinity and on the local wind forcing.

2. Methodology

In this study, we use 52 CTD/LADCP (Conductivity, Temperature, Depth/Lowered Acoustic Doppler Current Profiler) stations collected at the shelf break and continental slope between 2 February and 5 March 2014, from which we define five hydrographic sections (three cross-slope, quasi-meridional sections MS1-CT, MS2-CT and MS3-ET, and two cross-trough, quasi-zonal sections ZS5-CT and ZS6-ET; Figures 1a and 2). In addition, we use data from SADCP (shipboard ADCP; Figure 1a) and from five moorings deployed at the shelf break and within the central troughs of the eastern Amundsen Sea continental shelf (Figure 1; Table 1). Moorings M1-CT and M12-CT are co-located and thus considered as a single ~4-yr time series.

We estimated tidal current velocities empirically based on the harmonic analysis of the hourly mooring time series using the main tidal constituents in the region (semidiurnal and diurnal). These were then used to de-tide LADCP and SADCP currents. Tidal velocities derived from mooring M5-US were used for measurements onshore of the 1,000 m isobath and M1-CT and M20-ET for measurements over the continental shelf at central and eastern troughs, respectively. The average magnitude of the empirically derived tidal currents (0.01 m s^{-1}) is small compared to the representative core velocity of the onshore flow (approximately 0.1 m s^{-1}). In agreement with that, the de-tiding of LADCP and SADCP currents used to reference the geostrophic velocities had relatively little impact on the resulting fluxes.

All variables for both moorings and hydrographic sections were computed according to the International Thermodynamic Equation of Seawater-2010 (TEOS-10) framework (McDougall & Barker, 2011). Geostrophic shear was calculated for the five hydrographic sections (Figure 1a). For referencing shear, for each station pair, the method and depth range away from boundaries that gave vertical shear most similar to geostrophic shear was chosen from: (a) using one of the two cross-section LADCP velocity profiles; (b) the average of the two cross-section LADCP profiles or (c) the SADCP cross-section velocities averaged between the CTD stations. In the majority of cases (69%), the averaged LADCP profiles were used to reference the geostrophic shear, and in 24% of the cases, the averaged SADCP gave the best match.

For the cross-section geostrophic transport calculations, the velocity in the bottom triangle was extrapolated following Thompson and Heywood (2008). The error in the transport estimate for each hydrographic section was calculated by applying the Monte Carlo technique where, through an iterative process, a random number from a normal distribution (mean and sigma equal to 0 and 0.05) was added to each geostrophic velocity profile. The reported error is the standard deviation of the transports estimated using velocities from 1,000 Monte Carlo realizations.

Cross-section quasi-heat transport (Q_h) was then calculated from:

$$Q_h = C_p \int_D^0 \int_{x_1}^{x_n} \rho \cdot V \cdot T_r \, dz \, dx; \tag{1}$$

where x is the horizontal coordinate (m) along the section, D is the water column depth (m) over which the integration is performed, C_p (3,985 J K^{-1} kg^{-1}) is the seawater-specific heat capacity, ρ is the in-situ density, V ($m\,s^{-1}$) is cross-section absolute geostrophic velocity and $T_r = T - T_0$ is temperature minus a reference temperature. Following Walker et al. (2007), we use the surface freezing point of water with the salinity of CDW as a reference temperature, thus obtaining a quasi-heat transport representing the amount of energy available for melting ice. We refer to this calculation as quasi-heat transport because the net volume flux across each section is non-zero. We quantify the volume and quasi-heat transport for all waters denser than the neutral density isopycnal $\gamma^n = 28$ kg m^{-3}, which is the lowest density bound of CDW in the Amundsen Sea (Arneborg et al., 2012; Whitworth et al., 1998).

For each mooring, the current velocities were rotated using an angle defined based on bathymetry (Figure 1b). For the moorings inside the troughs, the new coordinate system was rotated to give an along-trough component (positive onshore). For M5-US, we also evaluate the along-slope component (positive eastward). For this mooring, the angle of rotation for the new coordinate system was chosen so that the along-slope velocity component followed the continental slope isobaths.

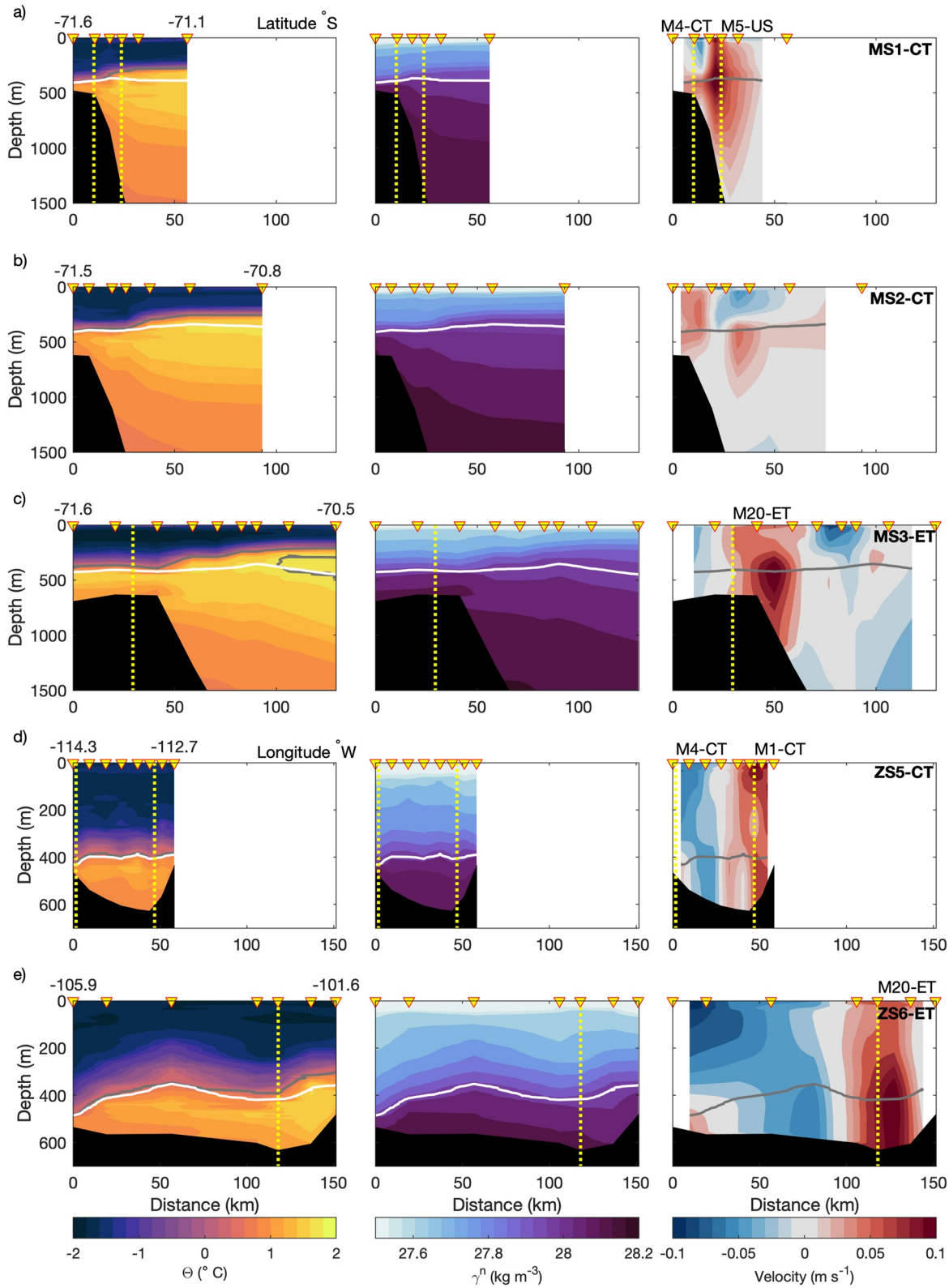

Figure 2. Conservative temperature (Θ; °C, left), neutral density (γ^n; kg m^{-3}, center) and absolute geostrophic velocity (m s^{-1}, right; positive values indicate eastward/southward flow) for meridional sections (a) MS1-CT, (b) MS2-CT, (c) MS3-ET, and zonal sections (d) ZS5-CT, (e) ZS6-ET. Vertical dashed yellow lines indicate labeled mooring positions, and yellow triangles the CTD stations. On the left panels, 1.8°C and 0.5°C isotherms are highlighted by thick and thin gray contours. The 28 kg.m^{-3} isopycnal is highlighted by white contours on the left and center panels, and by gray contours on the right panels.

Table 1
Summary of Current Meter Instruments Used in This Study, Their Average Depths and Sampling Period at Each of the Moorings

Mooring	Sampling period	Position	Bottom depth (m)	Instrument	Depth of instruments (m)	Height above bottom (m)
M1-CT (iSTAR 1)	6 March 2012 to 2 March 2014	71°S 33.7′; 113°W 02.7′	605	ADCP 75 kHz	497.7	145
				Aquadopp	587.5	24
M12-CT (trough_w)	2 March 2014 to 7 February 2016	71°S 33.7′; 113°W 02.7′	605	Aquadopp	423	182
				Aquadopp	555	50
M4-CT (iSTAR 4)	5 March 2012 to 28 February 2014	71°S 32.7′; 114°W 18.2′	513	Aquadopp	486	27
M5-US (iSTAR 5)	5 March 2012 to 28 February 2014	71°S 25.4′; 114°W 18.9′	1,465	Aquadopp	399	1,066
				Aquadopp	559	906
				Aquadopp	718	747
M20-ET (trough_e)	4 March 2014 to 4 February 2016	71°S 19.7′; 102°W 33.0′	634	Aquadopp	467	167
				Aquadopp	595	39

Note. Mooring's original names, as listed in the cruise reports and data centers, are indicated in parentheses. Depths of temperature measuring instruments from moorings M1/M12-CT and M5-US are shown in Figures 4c and 5c.

Conservative temperature and along-trough/-slope velocities were daily averaged from an original sampling resolution of 10 min and vertically interpolated to a 10 m grid between the minimum and maximum depths of available temperature measurements at each mooring (M1/M12-CT: 332 and 552 m, M4-CT: 361 and 481 m; M5-US: 309 and 719 m; M20: 378 and 595 m). The interpolated fields were used to quantify the daily heat flux time series (HF; W m^{-1}) as follows:

$$HF_{(t)} = C_p \cdot \rho_0 \int_{D_2}^{D_1} V_{(t)} \cdot T_{r(t)}\, dz; \tag{2}$$

where $V_{(t)}$ and $T_{r(t)}$ are daily interpolated values. We also quantify the component of the HF depending on velocity variability $\left(V' \cdot \overline{T}\right)$ and the one depending on the temperature variability $\left(\overline{V} \cdot T'\right)$, where an overbar indicates the time mean over the record length and a prime indicates a deviation from the time mean. The moorings do not cover the entire water column and there are periods in which the thermocline is shallower than the instruments, thus part of the high-frequency variability associated with the thermocline is missed. However, since the surface waters are close to the freezing temperature, the resulting errors in the HF calculations are comparatively small (Ha et al., 2014).

Monthly averages for each mooring sampling period revealed a seasonal cycle that is weak for along-trough flow and well-defined for along-slope flow at the shelf break, with highest velocities in June, and lowest velocities in November–February (not shown). For water masses in the central trough, the seasonal cycle is characterized by colder waters and deeper thermocline in austral spring and the beginning of austral summer (October–January; not shown). This is similar that observed further onshore in Pine Island Bay (Mallett et al., 2018; Webber et al., 2017), and in models (e.g., Dotto et al., 2019). Based on this analysis, we removed the seasonal cycle, estimated by daily interpolation of monthly mean values, from HC, velocity and HF time series before analysis of correlations and wavelets. For correlation analysis, time series were also smoothed with a 30-day running mean filter. The same data processing was applied to ERA-Interim (Dee et al., 2011) zonal wind stress (τ_U) and wind stress curl ($\nabla \times \tau$). All correlation coefficients between single time series reported here are statistically significant at the 95% level (p-value <0.05). The wavelet (Morlet wavelets, following Torrence & Compo, 1998) and wavelet coherence (Grinsted et al., 2004) analyses were done for periods between 2 days and 8 months for HF and ERA-Interim τ_U and $\nabla \times \tau$.

3. Transport From CTD Sections

3.1. Cross-Slope Sections

In all sections, a surface-intensified westward flow is present near the shelf break, together with a subsurface-intensified eastward flow located between the shelf break (500–600 m) and the 2,000 m isobath (Figures 2a–2c). The position and strength of these currents vary among the sections. Between the shelf break and the 2,000 m isobath, both the CDW ($\gamma^n > 28$ kg m^{-3}) volume and along-slope quasi-heat transport decrease from the western side of the central trough (MS1-CT = 0.5 ± 0.2 Sv and 7.7 ± 2.3 TW) to the eastern side (MS2-CT = 0.05 ± 0.04 Sv and 4 ± 4 TW) and increase again further east, at the eastern trough (MS3-ET = 0.5 ± 0.2 Sv and 10.2 ± 2.6 TW). The observed decrease in the eastward flow from the western side to the eastern side of the central trough and partial recovery farther east are also described by Walker et al. (2013). This is consistent with modeling studies that show most of the flow turning cyclonically to enter the trough (Assmann et al., 2013; Kimura et al., 2017). The presence of an eastward undercurrent at the continental slope from our 2014 observations similar to that described from 2003 observations (Walker et al., 2013) suggests that this is a persistent feature, consistent with modeling studies (e.g., Assmann et al., 2013; Kimura et al., 2017).

3.2. Cross-Trough Sections

The inflow of CDW onto the continental shelf is at the eastern and deepest (~600 m) side of both central and eastern troughs, while the outflow of colder and deeper mCDW is at the western side of each trough (ZS5-CT and ZS6-ET; Figures 2d and 2e). Despite the higher velocities of CDW inflow at the eastern trough than at the central trough, both inflows show similar total CDW transport (0.09 ± 0.05 Sv) onto the shelf. Thus, the central and eastern troughs made similar contributions to the total transport of CDW that penetrates south onto the continental shelf, at least during the cruise period.

Despite the similar contribution in terms of volume transport, the quasi-heat transport estimated for the eastern trough (1.79 ± 0.7 TW) is higher than the central trough (1.21 ± 0.2 TW). This is due to the warmer temperature maximum and shallower thermocline in the eastern trough (the temperature maximum of waters onshore of the 650 m isobath is approximately 1.27°C at the central trough and 1.5°C at the eastern trough; Figures 2d and 2e and Figures 3a and 3b).

The onshore cumulative volume and quasi-heat transport estimated for the CDW layer at the central trough are lower than the estimates made by Walker et al. (2007) using CTD sections in March 2003 (0.23 ± 0.062 Sv and 2.8 ± 0.68 TW). However, the mooring records show that the 2014 cruise coincided with a period of relatively cold temperatures (Figure 4b) and weak onshore velocities (Figure 4a), so this difference is unlikely to indicate a long-term trend. Our snapshot estimates of volume and heat transport are also lower than model estimates of climatological onshore quasi-heat transport at the central trough (2.5 TW; Kimura et al., 2017). Our observations confirm the previously established current pattern in the central trough, but demonstrate that there is considerable variability in the onshore flow of CDW and associated heat transport.

4. Mechanisms Driving Temporal Variability in Mooring Observations

4.1. Interannual Variability of Water Mass Distribution and Circulation Pattern

The longest mooring time series (consecutive moorings M1/M12-CT; Figures 1b, 2d, and 4) is located in the eastern part of the central trough and captures the on-shelf flow of CDW. At the western flank of the central trough, mooring M4-CT captures mostly the off-shelf flow of mCDW (Figures 1b and 2d). Offshore of the shelf break, mooring M5-US (Figures 1b, 2, and 5) samples the upper slope current system, which was characterized by a strong subsurface eastward flow during the occupation of the CTD stations. The average direction of the flow at M5-US is southeastward, suggesting it captures the undercurrent turning and entering the central trough carrying warm waters onto the shelf (Figure 1b; St-Laurent et al., 2013; Walker et al., 2013).

At the eastern trough, the mean flow measured by mooring M20-ET is not fully aligned with the trough direction (Figure 1c), in contrast to the inflow at the central trough (M1/M12-CT; Figure 1b). This is likely because mooring M20-ET is close enough to the shelf break to capture the current rotating cyclonically to enter the narrow channel at the eastern portion of the trough, as shown by modeling studies (e.g., Assmann et al., 2013; Kimura

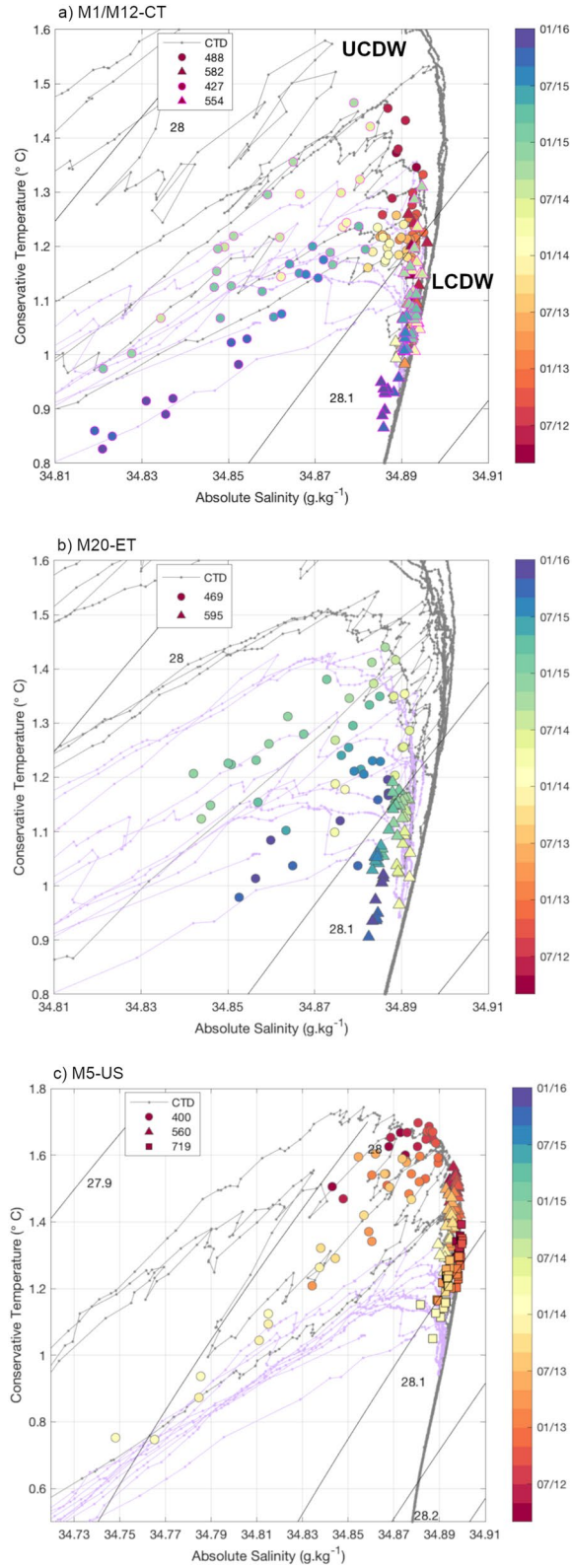

Figure 3. Conservative temperature (Θ)–absolute salinity (S_A) diagrams colored by time, from 15-day average of instruments on moorings (a) M1-CT and M12-CT (highlighted by markers with pink borders), (b) M20-ET, and (c) M5-US. Legend indicates instruments depth. CTD data from 2014 are shown for sections MS2-CT and ZS5-CT in (a), MS3-ET in (b), and MS1-CT in (c). Purple and gray CTD lines are stations onshore and offshore of 600 m, respectively. Contours show neutral density (γ^n) surfaces. Axes of panels (a and b) are expanded compared with panel (c).

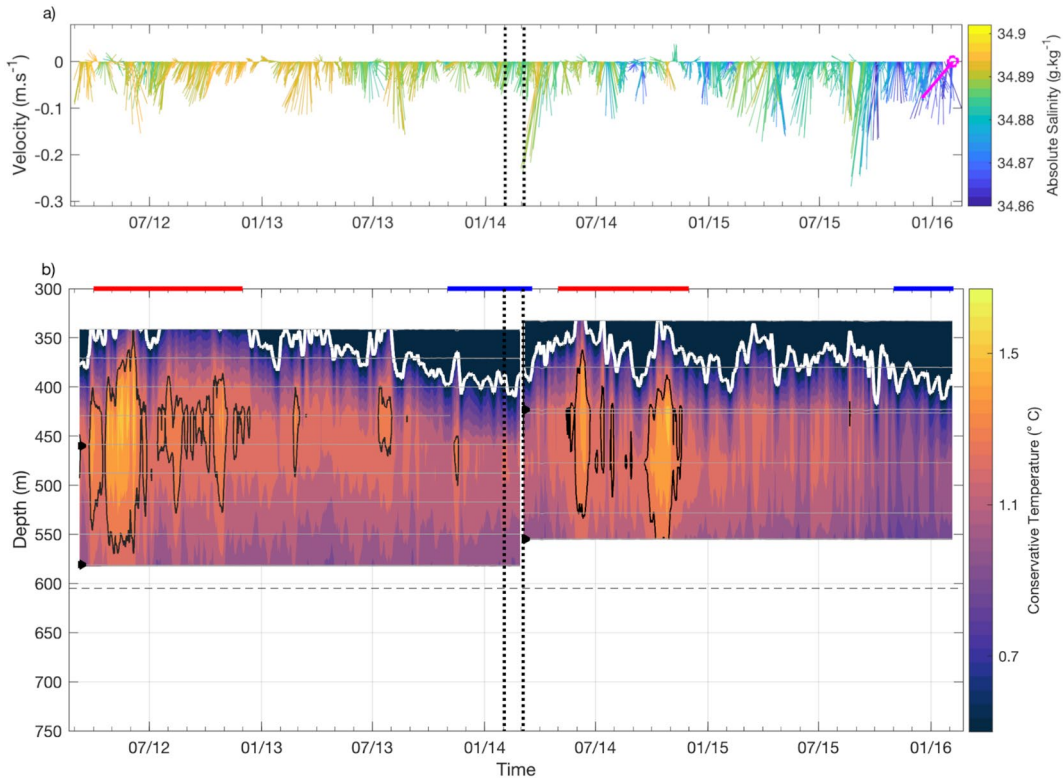

Figure 4. Moorings M1/M12-CT (a) velocity (m s^{-1}) colored by absolute salinity, both averaged between 490 and 550 m. Pink arrow indicates direction of the along-trough axis for reference. Velocity and arrow scale follow the *y*-axis, which is aligned with the along-trough direction. Pink arrow shows "south" direction in the NSEW coordinate system. (b) Conservative temperature (Θ; °C) time series, with 0.5°C (white), and 1.3°C (black) isotherms superimposed. Horizontal gray lines indicate depths of temperature measuring instruments. Black triangles indicate depth of current meters. Horizontal gray dashed line shows the local sea bed depth (m). Horizontal red and blue lines indicate "warm" and "cold" periods as defined in text. Dashed vertical lines indicate the cruise period. Daily time series are smoothed using a low-pass 6-day filter for plotting clarity.

et al., 2017; Webber et al., 2019). Therefore, we argue that, despite the strong eastward component, the flow at M20-ET mostly captures the on-shelf flow of warm waters.

The import of CDW onto the shelf, and its associated flux of heat, is indicated as a predictor of basal melt (Holland et al., 2019; Jenkins et al., 2018). Variations in the CDW HF onto the shelf can be due to changes either in the thermocline depth, or in the velocity below the thermocline, or both. Insights on the nature of changes in both of these quantities will improve understanding of the dynamics leading to variability of HF. Mooring M1/M12-CT shows two main inflow events of relatively warm ($1.3 < \Theta < 1.5$°C) and light ($28.1 < \gamma^n < 28.11$ kg m^{-3}) waters in winter/spring 2012 (April–November) and 2014 (April–June and October–November) with episodic intrusions of unmodified CDW ($\Theta > 1.5$°C; Figure 4b). In this region, a thermocline separates the cold surface waters ($\Theta < 0$°C) from the warmer CDW underneath (Walker et al., 2013). Placed within this transitional layer, $\Theta = 0.5$°C is used here to represent the depth of the thermocline (Figure 4b). After these warm periods, there is a gradual cooling of the CDW and a gradual deepening of the thermocline, leading to cold periods of minimum temperature and maximum thermocline depths during summer (November–March) 2013/2014 and summer 2015/2016. This places the cruise period (February–March 2014) in relatively cold ocean conditions as described by Dutrieux et al. (2014) and Jenkins et al. (2018). The period of lowest temperature is observed after September 2015 at M1/M12-CT and is associated with the lowest salinity values (Figures 3a and 4).

Moorings M5-US (Figure 5) and M4-CT (not shown) also show the period of warmer temperatures and shallower thermocline in winter/spring 2012 followed by the cooling and deepening thermocline into summer 2013/2014 observed at M1/M12-CT (Figure 4b). This suggests that variability in thermocline depth at M1/M12-CT between winter/spring 2012 and summer 2013/2014 is due to coherent temporal variability across the central trough

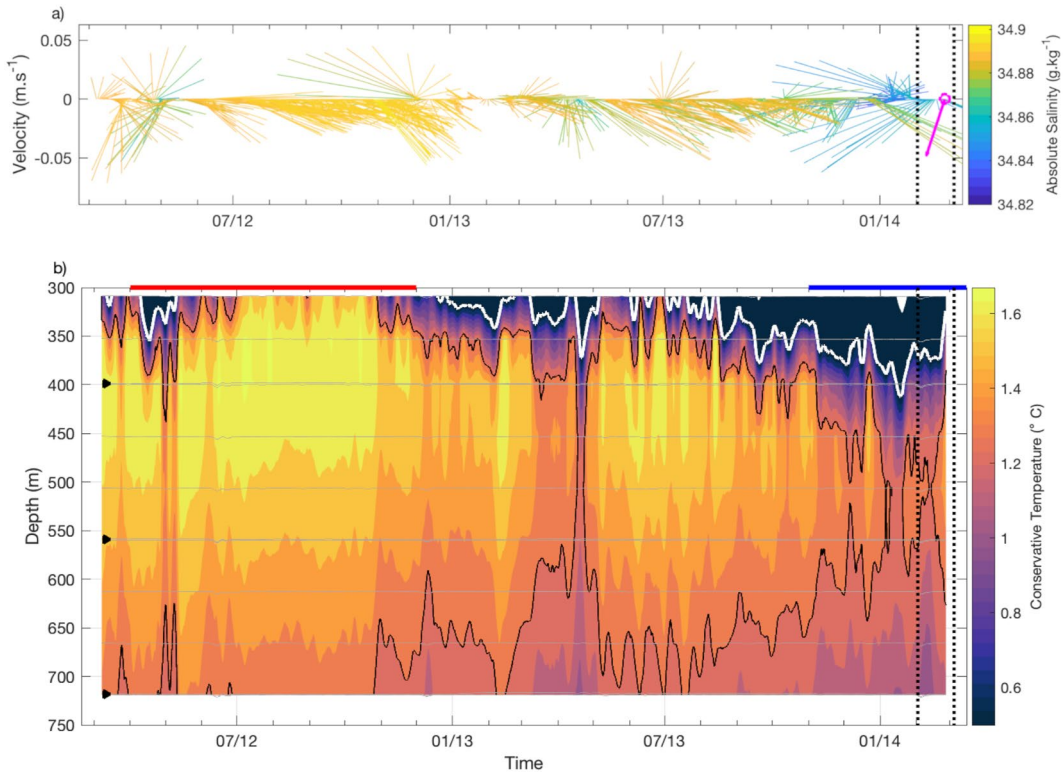

Figure 5. As Figure 4, but for mooring M5-US between depths 309–719 m.

area rather than lateral displacement of the warmer inflow and colder outflow to another location within the central trough. Similarly, the relatively cold conditions in summer 2015/2016 at M1/M12-CT are also observed at M20-ET in the eastern trough (Figure 3b), suggesting that these changes are part of a larger spatial scale variability. Consistent with changes in water temperature (Figure 3) and thermocline depths (Figures 4b and 5b), there is a coherent decrease in HC at all moorings between winter 2012 and summer 2013/2014 across the central trough area and shelf break, and between winter 2014 and summer 2015/2016 across the central and eastern troughs (Figure 6a).

Interannual variability is also observed in the moorings' velocities (Figure 6b), but it differs from the variability observed in heat content (Figure 6a). Between 2012 and 2014, none of the moorings show a consistent variation in the along-trough velocities, in contrast to the steady decrease in HC during this period (Figure 6a). Furthermore, after September 2014, changes in velocity are opposite to changes in heat content. The gradual increase of along-trough velocity at the central and eastern troughs after their minima in September 2014 (Figure 6b) contrasts with the simultaneous decrease of HC observed at both troughs (Figure 6a). HC and along-trough velocities are negatively correlated at M12-CT and M20-ET ($r = -0.43$ and $r = -0.58$, respectively), indicating stronger onshore flow coincident with lower HC.

At the shelf break (M5-US), the period characterized by the strongest negative along-slope velocities (summer 2013/2014; Figures 5a and 6b) is coincident with the lowest HC within the M5-US sampling period (Figure 6a), which is linked to a deeper thermocline, freshening and cooling (Figures 3c and 5) of the upper 700 m of the water column. We return to the possible reasons for this relationship in Section 5.

Water mass properties show distinct differences between on- and offshore CTD stations, which can help to explain the dynamics and nature of the changes in HC and temperature that we see in the mooring records (Figure 3). For example, at M5-US (Figure 3c), the 400 m depth measurements at the start of the record (dark red circles, early 2012) overlie the offshore temperature maximum. At the same time, deeper measurements (dark red triangles and squares) are also consistent with offshore (gray) CTD profiles. In contrast, by the end of the record (yellow points, early 2014), measurements at all depths are more consistent with colder, fresher, more onshore CTD profiles. During the transition between these states, temperature decreases at all instrument depths, but

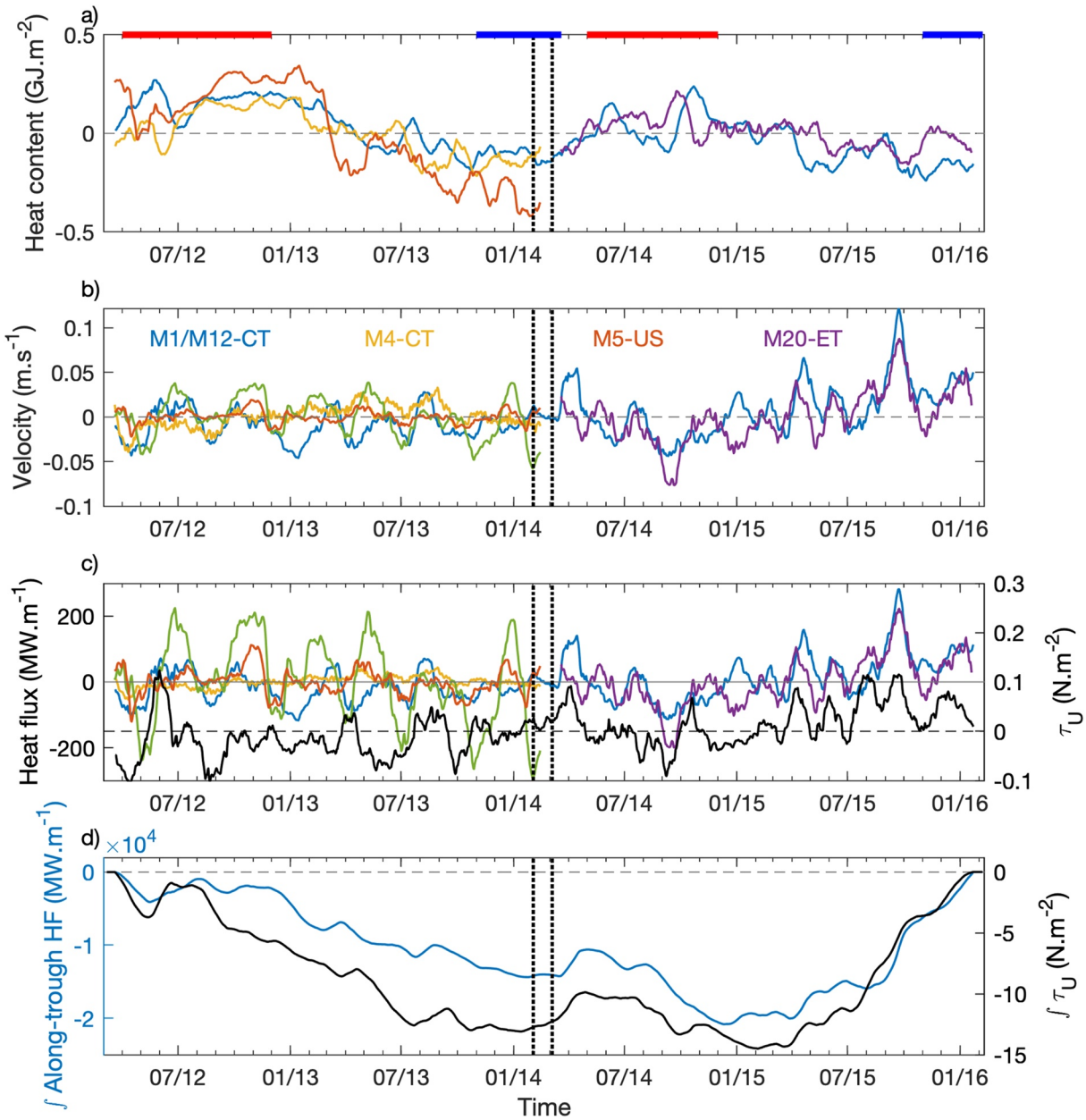

Figure 6. (a) Heat content (J m^{-2}) and (b) depth-averaged along-trough velocity (m s^{-1}; positive values indicate onshore flow; see Table 1 for depth ranges) from moorings M1/M12-CT (blue), M4-CT (yellow), M5-US (orange), and M20-ET (purple). Panel (b) also shows along-slope velocity component at M5-US (green line). Panel (c) presents along-trough heat flux (HF; MW m^{-1}) from each mooring, following same colors and integrated between same depths as in panel (b). Black line shows zonal wind stress (τ_U N m^{-2}; positive eastward; right-hand *y*-axis) from ERA-Interim reanalysis, averaged within yellow box in Figure 7. (d) Time-cumulative along-trough HF (MW m^{-1}) from mooring M1/M12-CT (blue line) and time-cumulative ERA-Interim zonal wind stress (τ_U N m^{-2}; positive eastward). In all panels, daily time series are deseasonalized and smoothed with a 30-day low pass filter. Vertical dashed lines indicate the cruise period. Horizontal red and blue lines indicate "warm" and "cold" periods as defined in text.

density increases at the deeper instruments (depth 560 and 719 m, Figure 3c) while decreasing at 400 m (circles in Figure 3c). These colder and denser measurements at deeper instruments suggest the presence of a deeper variety of CDW. All of these changes are consistent with a shift in the meridional gradients of temperature, salinity, and density evident at MS1-CT (Figure 2a), suggesting an offshore movement of the slope front.

Similarly to M5-US, the coldest conditions observed at the other moorings (Figures 3a and 3b) are all consistent with a shift to more onshore water mass properties, although the changes are less clear since the offshore water does not typically reach these moorings. Nevertheless, a transition toward a fresher, colder, and deeper CDW

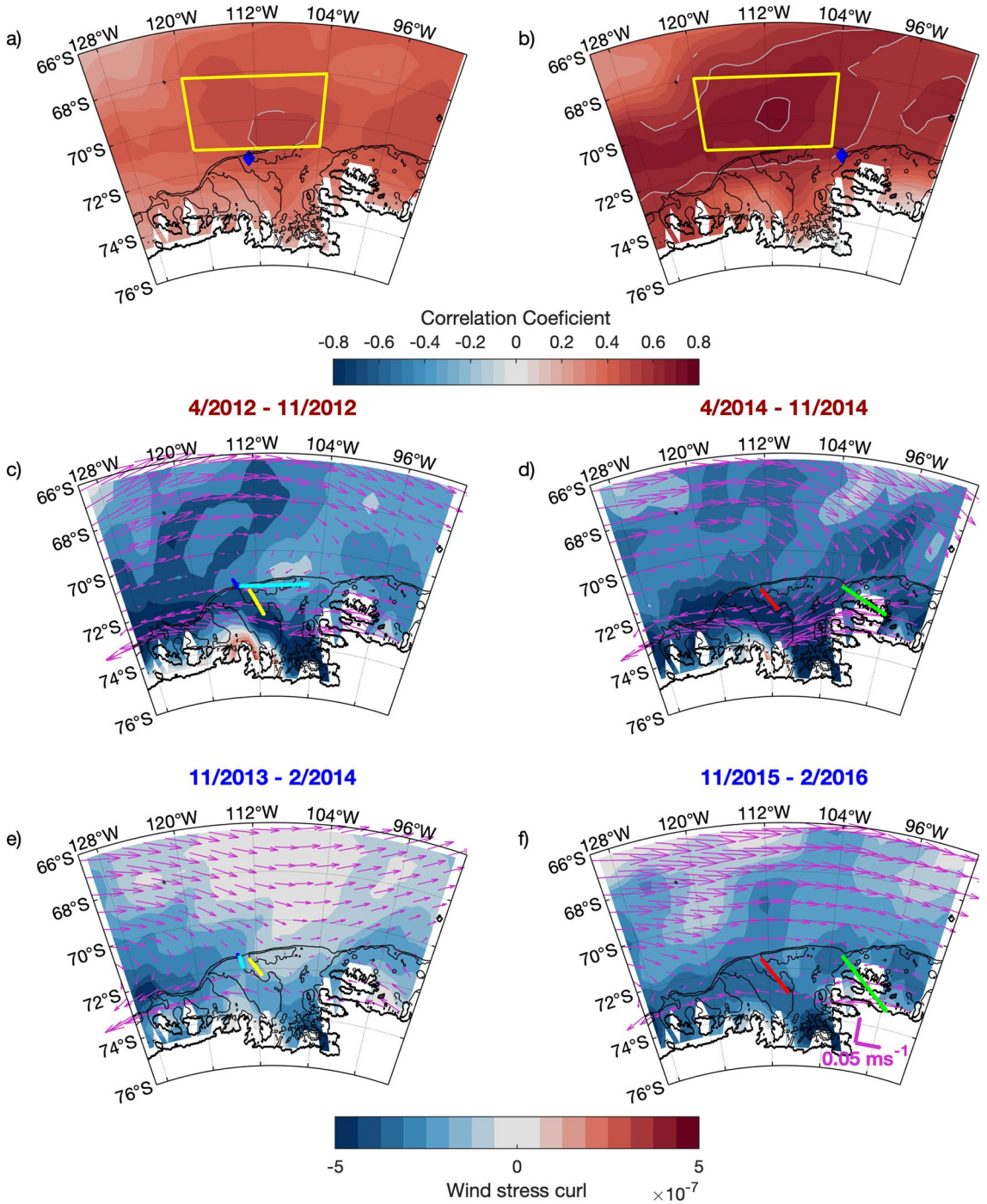

Figure 7. Correlation coefficient (r) between ERA-Interim zonal wind stress (τ_U; N m^{-2}) and along-trough HF (MW m^{-1}) at moorings (a) M1/M12-CT and (b) M20-ET. In panels (a and b) daily time series are deseasonalized and smoothed with a 30-day low pass filter. Areas of statistically significant correlation (p-value <0.15) are highlighted by gray contours. Yellow rectangle indicates area of high correlation over which wind stress was averaged for wavelet coherence calculation (Figure 8). Moorings location are marked by the blue dots. Maps showing ERA-Interim wind stress curl (N m^{-3}; shaded) and wind stress vectors (N m^{-2}; pink arrows) averaged for the relatively warm periods of (c) winter/spring 2012 (April–November 2012), (d) winter/spring 2014 (April–November 2014) and relatively cold periods of (e) summer 2013/2014 (November 2013–February 2014) and (f) summer 2015/2016 (November 2015–February 2016). Each mooring's average HF for the respective period is shown by arrows in dark blue (M4-CT), light blue (M5-US), yellow (M1-CT), red (M12-CT), and green (M20-ET). Black solid lines representing the 500 and 1,000 m isobaths (from BedMachine v2; Morlighem et al., 2020).

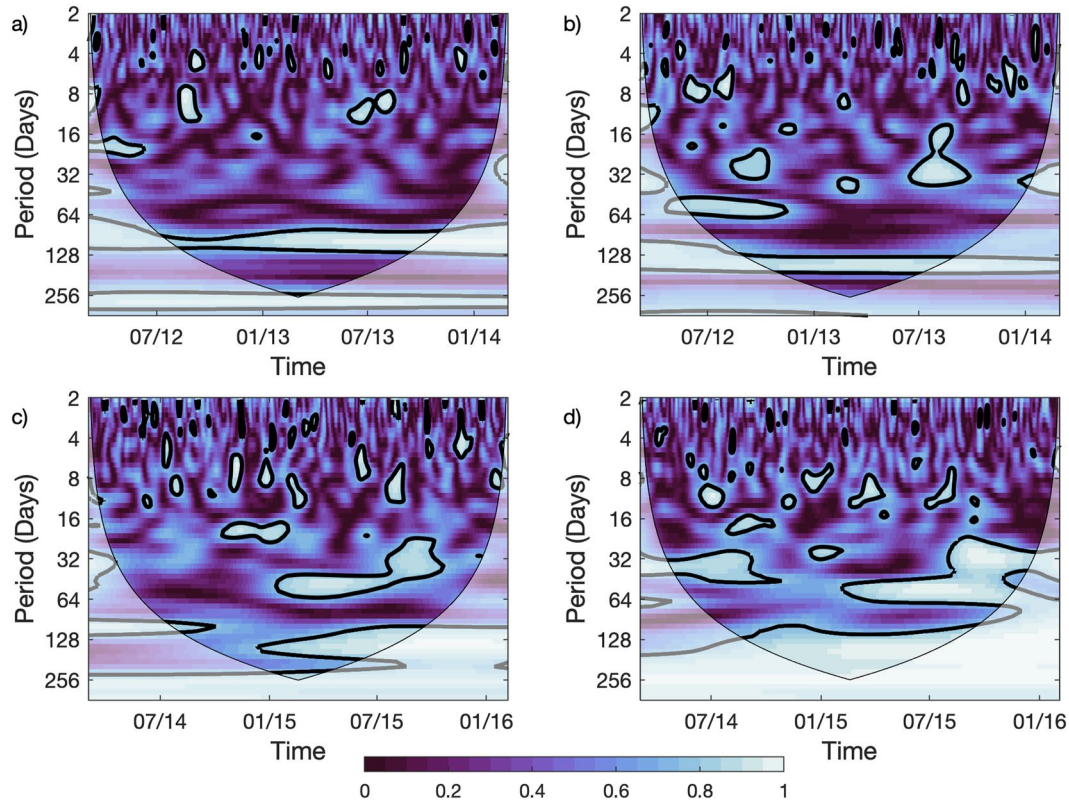

Figure 8. Wavelet coherence between daily deseasonalized time series of (a) ERA-Interim wind stress curl ($N\,m^{-3}$) and along-slope heat flux at mooring M5-US. Wavelet coherence of zonal wind stress ($N\,m^{-2}$) and along-through HF at moorings (b) M1-CT, (c) M12-CT, and (d) M20-ET. Zonal wind stress and wind stress curl anomaly time series were averaged within the box defined in Figure 7a, identified as area of high correlation between HF and wind stress. Black contours enclose regions of greater than 95% confidence level against red noise. The lighter shade areas mark the cone of influence, where edge effects are likely present.

variety is evident by the end of the M1/M12-CT and M20-ET mooring records at the relatively deep instruments (dark blue triangles in Figures 3a and 3b). While the CTD 2014 on-shore temperature maxima (Figure 3a) are within the range observed in historical data sets (e.g., Figure 2d of Dutrieux et al., 2014) at the central trough, the variation observed at the mooring instruments at similar depths and location (M12-CT in Figure 3a) is greater. These atypical variations and the diverging density changes between deep and shallow instruments at M1/M12-CT and M20-ET (dark blue points in Figures 3a and 3b) are consistent with offshore movement of the slope front and the warmer, lighter CDW core; this frontal movement is in turn associated with upwelling of a colder CDW variety in the bottom Ekman layer.

4.2. Variability of Heat Flux

We assess the impact of the variability in the flow of warm water onto the continental shelf by quantifying its HF and its components ($V' \cdot \overline{T}$ and $\overline{V} \cdot T'$). High correlation coefficients (r above 0.9 in all moorings) between the along-trough HF daily time series and $V' \cdot \overline{T}$ indicates that the along-trough HF variability is primarily controlled by velocity, in agreement with previous studies (e.g., Assmann et al., 2013; Webber et al., 2019). Consistent with this, the observed warm and cold periods (e.g., Figure 4b) do not seem to strongly modulate the HF estimated for the moorings inside the troughs (Figure 6c). Instead, HF time series broadly follow the variations observed in velocity (Figure 6b), increasing in line with the velocities after mid-2014 and with consistently high values during the El Niño period of 2015–2016. Most noticeable is the overall increase in the along-trough HF at M1/M12-CT and M20-ET between September 2014 and September 2015 (Figure 6c), consistent with the increase in along-trough velocity (Figure 6b). Thus, the increase in flow velocity during 2014–2016 was the dominant driver of onshore HF variability.

4.3. Co-Variability of Heat Fluxes

For the central trough, we would expect current velocity and, consequently, the HF time series to show some degree of covariance between mooring locations based on our understanding of the current pattern and dynamics. However, we find weak correlations between the HF time series for the moorings around the central trough. For example, correlations for both the along-slope and along-trough HF time series at M5-US with the M1-CT along-trough HF do not exceed $r = 0.3$ (maximum at zero lag, correlations calculated lagging time series for up to 60 days). These correlations between the HF at different moorings in the central trough are lower than the correlations between the HC time series (correlations between 0.5 and 0.65). This is perhaps not surprising since the flows and HF time series are very variable compared with the HC. Nevertheless, it demonstrates relatively weak coherence in the strength of the flow of CDW along the slope and onto the continental shelf at these locations.

The highest correlation between HF time series occurs between the along-trough components from central (M12-CT) and eastern (M20-ET) troughs at short lags (2 days lag; $r = 0.65$). This high correlation is partially due to the coherent lifting and deepening of the CDW layer, which affects the HC and the HF. For example, both troughs experienced simultaneously the period of warmer waters and shallower thermocline (winter/spring of 2014), followed by the cooling and deepening of thermocline (summer 2015/2016). However, while the correlation between the HC at the central (M12-CT) and eastern (M20-ET) troughs is significant ($r = 0.34$), it is lower than the HF and velocity correlation ($r = 0.65$ and $r = 0.66$, respectively), in contrast with moorings in the vicinity of the central trough (e.g., M5-US and M1-CT). This demonstrates that the correlation calculated between HF at the central and eastern troughs is primarily dictated by current dynamics rather than temperature changes. Moreover, the velocity-driven interannual changes in the along-trough HF, observed simultaneously at both troughs after September 2014, also support this dynamical link between the troughs, which could occur as a response to the same surface wind forcing. This high correlation is noteworthy since modeling studies have shown inconsistency or heterogeneity between the responses in these troughs to changes in atmospheric forcing (e.g., Dotto et al., 2019; Kimura et al., 2017; Webber et al., 2019).

4.4. Influence of Local Winds on Heat Flux Variability

Given the co-variability between the two troughs, we now investigate the role of the wind forcing driving the HF in both locations, using maps of correlation between HF and zonal wind stress (τ_U; Figure 7a) and wind stress curl ($\nabla \times \tau$; Figure 7b) from ERA-Interim reanalysis (Dee et al., 2011). At all moorings, except for M5-US, the along-trough HF is more strongly correlated with τ_U (e.g., at M1/M12-CT; Figure 7a) than $\nabla \times \tau$ (not shown), consistent with previous studies (e.g., Assmann et al., 2013). The along-slope HF at the shelf break (M5-US) is more strongly correlated with $\nabla \times \tau$ ((not shown). The area of highest correlation ($r > 0.45$) between the M1/M12-CT HF time series and the wind stress field is just north of the shelf break (Figure 7a). This area of highest correlation is similar to M20-ET (Figure 7b) and indicates a positive relationship between eastward wind stress anomalies just north of the shelf break and onshore HF at the central and eastern troughs. Based on the correlation maps, we selected the area of high correlation as defined by the yellow box in Figure 7a and averaged τ_U within that area to estimate its lagged correlation with HF from each mooring. Averaged τ_U is most strongly correlated with the along-trough HF time series from M12-CT and M20-ET of all moorings ($r = 0.5$ and $r = 0.7$ respectively, at lag 0). This suggests a strong relationship between local winds and onshore HF at both central and eastern troughs between 2014 and 2016.

The coherence between $\nabla \times \tau$ and along-slope HF at M5-US (Figure 8a), and between τ_U and along-trough HF at M1-CT (Figure 8b), are highest at periods of 90–130 days (3–4 months). This suggests that during 2012–2014, the HF associated with the along-slope flow and with the onshore flow in the central trough is associated with the variability of the local wind forcing at inter-monthly (3–4 months) time scales. For both M12-CT (central trough) and M20-ET (eastern trough) along-trough HF time series, the covariance with τ_U is strong at periods longer than 90 days (3 months) during most of their sampling period (2014–2016; Figures 8c and 8d). This, together with the strong correlation with wind stress found at both moorings, suggests an important role of local winds as drivers of variability of onshore HF at both central and eastern troughs at inter-monthly and potentially longer time scales.

The close relationship between local τ_U and along-trough HF at the central and eastern troughs is highlighted by their simultaneous increase after September 2014 (Figures 6c and 6d). This explains the strong correlation found between along-trough HF from these troughs ($r = 0.7$), which would be responding dynamically to large and

persistent changes in the zonal winds. Supporting this, the increase in along-trough HF at both troughs coincides with an increase in τ_U (Figures 6c and 6d). This increase in τ_U after September 2014 is consistent with the local response to the strong El Niño conditions that developed during 2015/2016 (Paolo et al., 2018). A hypothesized connection between tropical atmospheric anomalies, local winds, and warm water intrusion to the Amundsen Sea continental shelf has been explored by previous studies (e.g., Dutrieux et al., 2014; Steig et al., 2012; Thoma et al., 2008). Our results showing the coincident increase in onshore HF and τ_U after September 2014 are the first observational evidence of this hypothesized connection occurring at both central and eastern troughs as a simultaneous dynamic response to local and remote forcing.

5. Discussion

We have shown a relationship between local wind stress and the onshore heat flux at the Amundsen Sea central and eastern troughs at intermonthly time scales (e.g., Figure 8). This is consistent with previous studies relating wind stress anomalies at the shelf break area with CDW inflow onto the Amundsen Sea continental shelf on monthly to decadal time scales (e.g., Assmann et al., 2019; Dotto et al., 2020; Kimura et al., 2017; Spence et al., 2014; Thoma et al., 2008; Webber et al., 2019). At interannual time scales, this relationship is clearly demonstrated during the 2015/2016 El Niño year, when eastward wind anomalies associated with this event coincided with a strong increase in onshore HF at both the central and eastern troughs driven by stronger onshore flow (Figures 6b and 6c).

We hypothesize that the changes in hydrographic conditions observed in our data set during the anomalous 2015/2016 El Niño year can be explained by wind forcing affecting onshore flow through the mechanism proposed by Dotto et al. (2020), whereby an eastward wind anomaly drives a barotropic acceleration of the undercurrent by changing the meridional sea surface slope between the shelf and offshore. The stronger undercurrent then leads to uplifting of deeper isopycnals at the continental slope/shelf break by bottom Ekman dynamics (Wåhlin et al., 2012), consistent with the increase in density seen in the deep mooring records (Figure 3) and in the onshore flow (Figure 6b).

In contrast to the Dotson-Getz trough, where the uplifting of the isopycnals leads to warming of the continental shelf (Dotto et al., 2020), the Pine Island-Thwaites troughs (which include the central and eastern troughs) cool in response to stronger eastward winds. This occurs because in the former, the CDW temperature maximum is below the trough's depth, while in central and eastern troughs it is just above (~400 m) the depth of the troughs (~520 m; Figure 2) and thus has permanent access to the shelf. Therefore, isopycnal shoaling allows a deeper and colder CDW variety to have greater access to the shelf, while the warmer and lighter CDW variety is pushed away from the shelf break. The slope front would also be pushed offshore as, by definition, it is associated with the horizontal gradient of properties. These differences in the mechanisms taking place between western and eastern Amundsen Sea shelf break agrees with Paolo et al. (2018), who showed regional differences in the strength response of the West Antarctic Ice Sheet to ENSO. This highlights the need for deeper understanding and better observations of the mechanisms involved.

From the observations presented here, after March 2014 the undercurrent behavior can only be inferred from the coherent changes in hydrography and onshore flow, as there were no instruments at the slope in this period. However, our hypothesis outlined above, linking stronger eastward winds to stronger heat flux but colder conditions, is supported by several lines of evidence. First, the water masses transported onto the shelf fluctuate between warmer and colder CDW varieties (Figure 3), with strong eastward wind stress (Figure 6c) likely leading to increased bottom Ekman transport and resulting in stronger on-shelf transport of the deeper, cooler CDW variety (Figure 4). Heat transport from both the eastern and central trough moorings (Figures 6a and 6c) increases consistently with eastward wind stress, which is coherent across larger spatial scales than more local ocean processes such as eddies and topographically trapped waves (e.g., Darelius et al., 2009). Therefore, the mechanism proposed here explains how, under anomalous forcing conditions such as during the 2015/2016 El Niño, the increase on the onshore HF coincided with a colder deep layer and lower HC within both the central and eastern troughs (Figure 6a). This relationship highlights that, at the shelf break, HF rather than HC or thermocline depth should be used as a proxy for heat content over the shelf. It also emphasizes that velocity data is critical for understanding the dynamics in this region, but yet not very common.

While the mechanisms proposed in our hypothesis are consistent with the changes observed during 2014–2016, during 2012–2014 there were no evident changes in the onshore flow (and HF) that would explain the observed changes in heat content (Figures 6a and 6b). During the austral summer 2013/2014, the changes in HC and water properties at shelf break moorings are consistent with meridional movement of the front, with a colder and deeper CDW variety reaching the continental shelf at depth, a deeper thermocline on the slope and shelf and the lack of the core of warmer CDW variety on the shelf, as seen at M1 (Figure 4b). However, it is not clear in this case what drives the likely movement of the front. There is no evidence of strong eastward wind stress at the shelf break near the central trough, with relatively weak eastward wind stress at the shelf break only further east (Figures 7e and 7f). Also, our observations cannot be fully explained by upwelling dynamics, for example, with the prevalent eastward winds driving upwelling at the slope during cold periods, because this process would lift isopycnals whereas we observe the thermocline to deepen during cold periods (Figure 4b). But it is possible that the eastward wind stress to the north and the cyclonic wind stress curl at and north of the shelf break (Figure 7e) help to shift the front location. It is also possible that the mechanism is more complex and may depend on remote changes in ocean properties, perhaps driven by changes in ice-shelf melting (Jourdain et al., 2017; Webber et al., 2019), or changes in the strength of the Ross Gyre (Nakayama et al., 2018).

Such cross-slope movement of the front and associated eastward slope flow (Figure 2a) could explain why we see a southwestward flow at the shelf break mooring (M5-US; Figure 5a) during the cold and fresh periods: the mooring would be sampling the upper slope westward flow (Figure 2a) instead of the eastward current. This would also explain why the correlations between the along-slope current (M5-US) and the onshore current in the central trough (M1-CT) are relatively low, as M5-US would not sample the eastward slope flow continuously. High variability in the strength and position of the Antarctic Slope Current across the continental slope has previously been observed in other shelf regions in Antarctic (e.g., Azaneu et al., 2017), supporting this hypothesis. Nevertheless, further investigation into how the front location, onshore CDW flow and thermocline depth respond to various patterns of atmospheric forcing is required to fully understand the changes observed during 2012–2014.

The key quantity influencing ice shelf melt rate is the supply of heat into the cavity, that is, a combination of mid-depth ocean heat content (e.g., Dutrieux et al., 2014; Jenkins et al., 2016; Webber et al., 2017) and circulation strength (e.g., Jacobs et al., 2011). Model results suggest that it is the flux of heat and CDW onto the continental shelf, rather than the shelf break heat content and thermocline depth, that is the primary driver of variability in the supply of heat to ice shelf cavities (Webber et al., 2019). This is further supported by observations showing much larger changes in heat content in Pine Island Bay than evident at the shelf break (Dutrieux et al., 2014; Webber et al., 2017). As such, the relatively low HF observed at the shelf break throughout 2012 (Figure 6c) is in agreement with La Niña conditions in 2011 and agrees well with the low heat content and basal melt rate reported by Dutrieux et al. (2014) from observations in 2012 close to the ice shelf in Pine Island Bay. We therefore expect that the increased on-shore heat flux in 2015/2016 (Figure 6c) would lead to warmer on-shelf conditions, which is consistent with the unprecedented retreat in the Antarctic sea ice, including the Amundsen Sea, in austral spring of 2016 associated with atmospheric anomalies and ocean forcing (Stuecker et al., 2017; Turner et al., 2017).

Therefore, our results support the hypothesis that variability in zonal winds at the shelf break influences the flow of heat onto the continental shelves and toward the ice shelves, thus influencing the basal melting of ice shelves vulnerable to retreat. However, the main mechanism that led to the increase in heat transported onto the shelf observed between 2015 and 2016 does not involve a shoaling of the thermocline as suggested by previous modeling studies (Steig et al., 2012; Thoma et al., 2008; Webber et al., 2019), but likely an increased bottom Ekman transport of colder waters associated with a stronger flow. In the projected scenario of increased frequency of extreme El Niño events (Cai et al., 2014; Wang et al., 2017), it is critical to further investigate the mechanism through which ENSO-induced changes in surface winds influence onshore heat flux. Furthermore, the projected poleward migration of the westerlies is expected to increase this onshore heat flux (Holland et al., 2019), and may have contributed to warming over the past century (Naughten et al., 2022), so it is necessary to understand how such changes will manifest in order to monitor and predict them. Our results underline the importance of measuring and simulating onshore currents, not just ocean temperatures, at the shelf break, to understand such dynamics. Furthermore, fully understanding the dynamical response to changing surface wind stress requires an enhanced ocean observing system to fully capture the variability of the slope-current system and the currents across the continental shelf. These responses differ between the troughs in the Amundsen Sea, and these regional differences need to be accurately represented in models.

6. Conclusions

Our analysis demonstrates that the flux of heat onto the eastern Amundsen Sea continental shelf is coherent between different troughs and primarily driven by zonal wind stress. In contrast to previous studies, we find that onshore heat flux is anti-correlated with heat content in the Pine Island-Thwaites troughs: increased onshore flow of CDW and heat coincides with a deeper thermocline and a colder temperature maximum. The onshore flow, heat flux, and heat content are highly correlated between the central and eastern troughs, suggesting a role for large-scale forcing most likely in the form of surface wind stress. We hypothesize that the increase in zonal wind stress associated with the 2015/2016 El Niño event strengthened the eastward undercurrent and the onshore transport of a deeper, colder CDW variety in the bottom Ekman layer leading to an increase in the HF. The contrasting changes in heat content and heat flux highlight the need for a deeper understanding of the mechanisms through which surface winds modulate the heat potentially available for ice shelf basal melting. It also emphasizes that velocity data is critical for understanding the dynamics in this region, and thus the need to monitor onshore flow as well as ocean temperature at the shelf break. At the shelf break, we suggest that heat flux is more important than heat content for ultimately determining ice-shelf melt, since an increase in heat flux will likely increase both the temperature (assuming constant heat loss) and the velocity (assuming the onshore flow is connected to the cavity circulation) of water flowing into the ice-shelf cavities. Furthermore, the expected positive correlation between ENSO-related zonal wind anomalies and heat content is not evident for 2016, suggesting that the hypothesized link between ENSO and ice-shelf melt (Dutrieux et al., 2014; Steig et al., 2012) is not produced via changes in heat content, but instead via changes in onshore heat flux. Understanding and monitoring the onshore flux of heat is of critical importance in the context of the predicted increase in extreme El Niño events (Cai et al., 2014; Wang et al., 2017) and the projected poleward shift of the surface westerly winds due to climate change (Holland et al., 2019).

Data Availability Statement

Data from iSTAR moorings are archived at the British Oceanography Data Centre; BODC Series Reference Number 1748833.

Acknowledgments
M.V.C.A. was supported by a CAPES-Brazil Ph.D. scholarship (0876-14-3). B.G.M.W. and K.J.H. were supported by funding from the U.K. Natural Environment Research Council's iSTAR Programme through NERC Grant NE/J005703/1. The author thank all involved with RRS James Clark Ross cruise JR294/295 for making these observations possible. The oceanographic data collected as part of the iSTAR program are available from the British Oceanographic Data Centre (https://www.bodc.ac.uk/data/bodc_database/nodb/data_collection/6552/).

References

Arneborg, L., Wåhlin, A. K., Björk, G., Liljebladh, B., & Orsi, A. H. (2012). Persistent inflow of warm water onto the central Amundsen shelf. *Nature Geoscience*, *5*(12), 876–880. https://doi.org/10.1038/ngeo1644

Assmann, K. M., Darelius, E., Wåhlin, A. K., Kim, T. W., & Lee, S. H. (2019). Warm Circumpolar Deep Water at the Western Getz Ice Shelf Front, Antarctica. *Geophysical Research Letters*, *46*(2), 870–878. https://doi.org/10.1029/2018GL081354

Assmann, K. M., Jenkins, A., Shoosmith, D. R., Walker, D. P., Jacobs, S. S., & Nicholls, K. W. (2013). Variability of Circumpolar Deep Water transport onto the Amundsen Sea Continental shelf through a shelf break trough. *Journal of Geophysical Research: Oceans*, *118*(12), 6603–6620. https://doi.org/10.1002/2013JC008871

Azaneu, M. V. C., Heywood, K. J., Queste, B. Y., & Thompson, A. F. (2017). Variability of the Antarctic slope current system in the northwestern Weddell Sea. *Journal of Physical Oceanography*, *47*, (12), 2977–2997. https://doi.org/10.1175/JPO-D-17-0030.1

Cai, W., Borlace, S., Lengaigne, M., Van Rensch, P., Collins, M., Vecchi, G., et al. (2014). Increasing frequency of extreme El Niño events due to greenhouse warming. *Nature Climate Change*, *4*(2), 111–116. https://doi.org/10.1038/nclimate2100

Chavanne, C. P., Heywood, K. J., Nicholls, K. W., & Fer, I. (2010). Observations of the Antarctic Slope undercurrent in the Southeastern Weddell Sea. *Geophysical Research Letters*, *37*(13). https://doi.org/10.1029/2010GL043603

Darelius, E., Smedsrud, L. H., Østerhus, S., Foldvik, A., & Gammelsrød, T. (2009). Structure and variability of the Filchner overflow plume. *Tellus, Series A: Dynamic Meteorology and Oceanography*, *61*(3), 446–464. https://doi.org/10.1111/j.1600-0870.2009.00391.x

Davis, P. E., Jenkins, A., Nicholls, K. W., Brennan, P. V., Abrahamsen, E. P., Heywood, K. J., et al. (2018). Variability in basal melting beneath Pine Island Ice Shelf on weekly to monthly timescales. *Journal of Geophysical Research: Oceans*, *123*(11), 8655–8669. https://doi.org/10.1029/2018JC014464

Dee, D. P., Uppala, S. M., Simmons, A. J., Berrisford, P., Poli, P., Kobayashi, S., et al. (2011). The ERA-Interim reanalysis: Configuration and performance of the data assimilation system. *Quarterly Journal of the Royal Meteorological Society*, *137*(656), 553–597. https://doi.org/10.1002/qj.828

Dotto, T. S., Garabato, A. C., Bacon, S., Holland, P. R., Kimura, S., Firing, Y. L., et al. (2019). Wind-driven processes controlling oceanic heat delivery to the Amundsen Sea, Antarctica. *Journal of Physical Oceanography*, *49*(11), 2829–2849. https://doi.org/10.1175/JPO-D-19-0064.1

Dotto, T. S., Naveira Garabato, A. C., Wåhlin, A. K., Bacon, S., Holland, P. R., Kimura, S., et al. (2020). Control of the oceanic heat content of the Getz-Dotson Trough, Antarctica, by the Amundsen Sea Low. *Journal of Geophysical Research: Oceans*, *125*(8). https://doi.org/10.1029/2020JC016113

Dutrieux, P., De Rydt, J., Jenkins, A., Holland, P. R., Ha, H. K., Lee, S. H., et al. (2014). Strong sensitivity of Pine Island Ice-Shelf melting to climatic variability. *Science*, *343*(6167), 174–178. https://doi.org/10.1126/science.1244341

Grinsted, A., Moore, J. C., & Jevrejeva, S. (2004). Application of the cross wavelet transform and wavelet coherence to geophysical time series. *Nonlinear Processes in Geophysics*, *11*(4), 561–566. https://doi.org/10.5194/npg-11-561-2004

Ha, H. K., Wåhlin, A. K., Kim, T. W., Lee, S. H., Lee, J. H., Lee, H. J., et al. (2014). Circulation and modification of warm deep water on the Central Amundsen Shelf. *Journal of Physical Oceanography*, *44*(5), 1493–1501. https://doi.org/10.1175/JPO-D-13-0240.1

Heywood, K. J., Biddle, L. C., Boehme, L., Fedak, M., Dutrieux, P., Jenkins, A., et al. (2016). Between the devil and the deep blue sea: The role of the Amundsen Sea continental shelf in exchanges between ocean and ice shelves. *Oceanography*, *29*(4), 118–129. https://doi.org/10.5670/oceanog.2016.104

Holland, P. R., Bracegirdle, T. J., Dutrieux, P., Jenkins, A., & Steig, E. J. (2019). West Antarctic ice loss influenced by internal climate variability and anthropogenic forcing. *Nature Geoscience*, *12*(9), 718–724. https://doi.org/10.1038/s41561-019-0420-9

Jacobs, S. S., Jenkins, A., Giulivi, C. F., & Dutrieux, P. (2011). Stronger ocean circulation and increased melting under Pine Island Glacier Ice Shelf. *Nature Geoscience*, *4*(8), 519–523. https://doi.org/10.1038/ngeo1188

Jenkins, A., Dutrieux, P., Jacobs, S. S., McPhail, S. D., Perrett, J. R., Webb, A. T., & White, D. (2010). Observations beneath Pine Island Glacier in West Antarctica and implications for its retreat. *Nature Geoscience*, *3*(7), 468–472. https://doi.org/10.1038/ngeo890

Jenkins, A., Dutrieux, P., Jacobs, S., Steig, E., Gudmundsson, H., Smith, J., & Heywood, K. (2016). Decadal Ocean Forcing and Antarctic Ice Sheet Response: Lessons from the Amundsen Sea. *Oceanography*, *29*(4), 106–117. https://doi.org/10.5670/oceanog.2016.103

Jenkins, A., Shoosmith, D., Dutrieux, P., Jacobs, S., Kim, T. W., Lee, S. H., et al. (2018). West Antarctic Ice Sheet retreat in the Amundsen Sea driven by decadal oceanic variability. *Nature Geoscience*, *11*(10), 733–738. https://doi.org/10.1038/s41561-018-0207-4

Jourdain, N. C., Mathiot, P., Merino, N., Durand, G., Le Sommer, J., Spence, P., et al. (2017). Ocean circulation and sea-ice thinning induced by melting ice shelves in the Amundsen Sea. *Journal of Geophysical Research: Oceans*, *122*(3), 2550–2573. https://doi.org/10.1002/2016JC012509

Kim, T. W., Ha, H. K., Wåhlin, A. K., Lee, S. H., Kim, C. S., Lee, J. H., & Cho, Y. K. (2017). Is Ekman pumping responsible for the seasonal variation of warm Circumpolar Deep Water in the Amundsen Sea? *Continental Shelf Research*, *132*, 38–48. https://doi.org/10.1016/j.csr.2016.09.005

Kimura, S., Jenkins, A., Regan, H., Holland, P. R., Assmann, K. M., Whitt, D. B., et al. (2017). Oceanographic controls on the variability of ice-shelf basal melting and circulation of glacial meltwater in the Amundsen Sea Embayment, Antarctica. *Journal of Geophysical Research: Oceans*, *122*(12), 10131–10155. https://doi.org/10.1002/2017JC012926

Konrad, H., Shepherd, A., Gilbert, L., Hogg, A. E., McMillan, M., Muir, A., & Slater, T. (2018). Net retreat of Antarctic glacier grounding lines. *Nature Geoscience*, *11*(4), 258–262. https://doi.org/10.1038/s41561-018-0082-z

Mallett, H., Boehme, L., Fedak, M., Heywood, K. J., Stevens, D., & Roquet, F. (2018). Variation in the distribution and properties of Circumpolar Deep Water in the eastern Amundsen Sea, on seasonal timescales, using seal-borne tags. *Geophysical Research Letters*, *10*, 4982–4990. https://doi.org/10.1029/2018GL077430

McDougall, T. J., & Barker, P. M. (2011). Getting started with TEO-10 and the Gibbs Seawarer Oceanographic Toolbox. SCOR/IAPSO WG127. Retrieved from http://www.teos-10.org/

Morlighem, M., Rignot, E., Binder, T., Blankenship, D., Drews, R., Eagles, G., et al. (2020). Deep glacial troughs and stabilizing ridges unveiled beneath the margins of the Antarctic ice sheet. *Nature Geoscience*, *13*(2), 132–137. https://doi.org/10.1038/s41561-019-0510-8

Mouginot, J., Rignot, E., & Scheuchl, B. (2014). Sustained increase in ice discharge from the Amundsen Sea Embayment, West Antarctica, from 1973 to 2013. *Geophysical Research Letters*, *41*(5), 1576–1584. https://doi.org/10.1002/2013GL059069

Nakayama, Y., Menemenlis, D., Zhang, H., Schodlok, M., & Rignot, E. (2018). Origin of Circumpolar Deep Water intruding onto the Amundsen and Bellingshausen Sea continental shelves. *Nature Communications*, *9*(1), 1–9. https://doi.org/10.1038/s41467-018-05813-1

Nakayama, Y., Schröder, M., & Hellmer, H. H. (2013). From Circumpolar Deep Water to the glacial meltwater plume on the eastern Amundsen Shelf. *Deep-Sea Research Part I Oceanographic Research Papers*, *77*, 50–62. https://doi.org/10.1016/j.dsr.2013.04.001

Nakayama, Y., Timmermann, R., & Hellmer, H. (2019). Impact of West Antarctic Ice Shelf melting on the Southern Ocean Hydrography. *The Cryosphere Discussions*, 1–15. https://doi.org/10.5194/tc-2019-244

Naughten, K. A., Holland, P. R., Dutrieux, P., Kimura, S., Bett, D. T., & Jenkins, A. (2022). Simulated twentieth-century ocean warming in the Amundsen Sea, West Antarctica. *Geophysical Research Letters*, *49*(5). https://doi.org/10.1029/2021gl094566

Paolo, F. S., Padman, L., Fricker, H. A., Adusumilli, S., Howard, S., & Siegfried, M. R. (2018). Response of Pacific-sector Antarctic ice shelves to the El Niño/Southern Oscillation. *Nature Geoscience*, *11*(2), 121–126. https://doi.org/10.1038/s41561-017-0033-0

Rignot, E., Mouginot, J., Scheuchl, B., Van Den Broeke, M., Van Wessem, M. J., & Morlighem, M. (2019). Four decades of Antarctic ice sheet mass balance from 1979 to 2017. *Proceedings of the National Academy of Sciences of the United States of America*, *116*(4), 1095–1103. https://doi.org/10.1073/pnas.1812883116

Smith, B., Fricker, H. A., Gardner, A. S., Medley, B., Nilsson, J., Paolo, F. S., et al. (2020). Pervasive ice sheet mass loss reflects competing ocean and atmosphere processes. *Science*, *368*(6496), 1239–1242. https://doi.org/10.1126/science.aaz5845

Spence, P., Griffies, S. M., England, M. H., Hogg, A. M., Saenko, O. A., & Jourdain, N. C. (2014). Rapid subsurface warming and circulation changes of Antarctic coastal waters by poleward shifting winds. *Geophysical Research Letters*, *41*(13), 4601–4610. https://doi.org/10.1002/2014GL060613

Steig, E. J., Ding, Q., Battisti, D. S., & Jenkins, A. (2012). Tropical forcing of Circumpolar Deep Water inflow and outlet glacier thinning in the Amundsen Sea embayment, west Antarctica. *Annals of Glaciology*, *53*(60), 19–28. https://doi.org/10.3189/2012AoG60A110

St-Laurent, P., Klinck, J. M., & Dinniman, M. S. (2013). On the role of coastal troughs in the circulation of warm Circumpolar Deep Water on Antarctic Shelves. *Journal of Physical Oceanography*, *43*(1), 51–64. https://doi.org/10.1175/JPO-D-11-0237.1

St-Laurent, P., Klinck, J. M., & Dinniman, M. S. (2015). Impact of local winter cooling on the melt of Pine Island Glacier, Antarctica. *Journal of Geophysical Research: Oceans*, *120*(10), 6718–6732. https://doi.org/10.1002/2015JC010709

Stuecker, M. F., Bitz, C. M., & Armour, K. C. (2017). Conditions leading to the unprecedented low Antarctic sea ice extent during the 2016 austral spring season. *Geophysical Research Letters*, *44*(17), 9008–9019. https://doi.org/10.1002/2017GL074691

Thoma, M., Jenkins, A., Holland, D., & Jacobs, S. (2008). Modeling Circumpolar Deep Water intrusions on the Amundsen Sea continental shelf, Antarctica. *Geophysical Research Letters*, *35*(18), 2–7. https://doi.org/10.1029/2008GL034939

Thompson, A. F., & Heywood, K. J. (2008). Frontal structure and transport in the northwestern Weddell Sea. *Deep-Sea Research Part I Oceanographic Research Papers*, *55*(10), 1229–1251. https://doi.org/10.1016/j.dsr.2008.06.001

Torrence, C., & Compo, G. P. (1998). A practical guide to wavelet analysis. *Bulletin of the American Meteorological Society*, *79*(1), 61–78. https://doi.org/10.1175/1520-0477(1998)079⟨0061:APGTWA⟩2.0.CO;2

Turner, J., Phillips, T., Marshall, G. J., Hosking, J. S., Pope, J. O., Bracegirdle, T. J., & Deb, P. (2017). Unprecedented springtime retreat of Antarctic sea ice in 2016. *Geophysical Research Letters*, *44*(13), 6868–6875. https://doi.org/10.1002/2017GL073656

Wåhlin, A. K., Muench, R. D., Arneborg, L., Björk, G., Ha, H. K., Lee, S. H., & Alsén, H. (2012). Some implications of Ekman layer dynamics for cross-shelf exchange in the Amundsen Sea. *Journal of Physical Oceanography*, *42*(9), 1461–1474. https://doi.org/10.1175/JPO-D-11-041.1

Walker, D. P., Brandon, M. A., Jenkins, A., Allen, J. T., Dowdeswell, J. A., & Evans, J. (2007). Oceanic heat transport onto the Amundsen Sea shelf through a submarine glacial trough. *Geophysical Research Letters*, *34*(2), 2–5. https://doi.org/10.1029/2006GL028154

Walker, D. P., Jenkins, A., Assmann, K. M., Shoosmith, D. R., & Brandon, M. A. (2013). Oceanographic observations at the shelf break of the Amundsen Sea, Antarctica. *Journal of Geophysical Research: Oceans*, *118*(6), 2906–2918. https://doi.org/10.1002/jgrc.20212

Wang, G., Cai, W., Gan, B., Wu, L., Santoso, A., Lin, X., et al. (2017). Continued increase of extreme El Ninõ frequency long after 1.5°C warming stabilization. *Nature Climate Change*, *7*(8), 568–572. https://doi.org/10.1038/NCLIMATE3351

Webber, B. G., Heywood, K. J., Stevens, D. P., & Assmann, K. M. (2019). The impact of overturning and horizontal circulation in Pine Island trough on ice shelf melt in the eastern Amundsen Sea. *Journal of Physical Oceanography*, *49*(1), 63–83. https://doi.org/10.1175/JPO-D-17-0213.1

Webber, B. G., Heywood, K. J., Stevens, D. P., Dutrieux, P., Abrahamsen, E. P., Jenkins, A., et al. (2017). Mechanisms driving variability in the ocean forcing of Pine Island Glacier. *Nature Communications*, *8*(1), 14507. https://doi.org/10.1038/ncomms14507

Whitworth, T., Orsi, A. H., Kim, S.-J., Nowlin, W. D., & Locarnini, R. A. (1998). Water masses and mixing near the Antarctic Slope Front. In S. S. Jacobs, & R. F. Weiss (Eds.), *Ocean, ice, and atmosphere: Interactions at the antarctic continental margin, antarctic research series* (Vol. 75, pp. 1–27). American Geophysical Union. https://doi.org/10.1029/AR075